



Direct Z-Scheme charge transfer in heterostructured MoO₃/g-C₃N₄ photocatalysts and the generation of active radicals in photocatalytic dye degradations*

Shengyang Xue ^{a, b}, Chunzheng Wu ^{b, c}, Shengyan Pu ^{a,*}, Yaqi Hou ^a, Tian Tong ^b, Guang Yang ^d, Zhaojun Qin ^{b, c}, Zhiming Wang ^c, Jiming Bao ^{b, c, d}

^a State Key Laboratory of Geohazard Prevention and Geoenvironment Protection (Chengdu University of Technology), Dongsanlu 1#, Exianqiao, Chengdu, 610059, Sichuan, PR China

^b Department of Electrical & Computer Engineering, University of Houston, Houston, TX, 77204, United States

^c Institute of Fundamental and Frontier Sciences, University of Electronic Science and Technology of China, Chengdu, 610064, China

^d Materials Science & Engineering, University of Houston, Houston, TX, 77204, United States

ARTICLE INFO

Article history:

Received 21 December 2018

Received in revised form

19 March 2019

Accepted 3 April 2019

Available online 6 April 2019

Keywords:

Graphitic carbon nitride

Molybdenum trioxide

Z-Scheme

Dye photodegradation

Superoxide radical

ABSTRACT

Photocatalytic degradation is an attractive strategy to purify waste water contaminated by macromolecular organics. Compared with the single-component photocatalysts, heterostructures of different semiconductors have been widely used to improve the photocatalytic performance. In this work, we fabricate a hetero-structured photocatalyst consisting of two-dimensional graphitic carbon nitride (g-C₃N₄) nanosheets and commercial MoO₃ microparticles through a simple mixing and annealing process. The photocatalytic performance was evaluated in various dye degradation reactions, especially Rhodamine (RhB) degradation. The MoO₃/g-C₃N₄ composite shown a significant improvement compared with individual MoO₃ or g-C₃N₄ as well as their physical mixture. By applying electron spin resonance (ESR) spin-trap spectra, radical scavenger experiments and electrochemical analysis, we find that a direct Z-scheme charge transfer between MoO₃ and g-C₃N₄ not only causes an accumulation of electrons in g-C₃N₄ and holes in MoO₃, but also boosts the formation of superoxide radical and hydroxyl radical. The superoxide radical and hole dominate the photocatalytic degradation, while the hydroxyl radical plays a negligible role and its production can be suppressed by lowering the pH value.

© 2019 Elsevier Ltd. All rights reserved.

1. Introduction

Dyes, as colored substance, have been widely used for textile, printing, and paper industries. Due to their high solubility in water and low biodegradability, a direct release of such wastes can lead to serious and long-term pollution of rivers and waterways. A variety of methods have been developed for water purification, such as membrane separation (Liao et al., 2018), physical adsorption (Pu et al., 2017a; Pu et al., 2018), chemical coagulation (Aljuboori et al., 2015), electrochemical (de Araujo et al., 2015) and biological activated sludge process (Grandclément et al., 2017). These methods transfer contaminants from water to another material

without degrading them into small and nontoxic molecules, leading to a secondary pollution. Advanced oxidation technology (Merkulov et al., 2018; Pu et al., 2017b; Pu et al., 2017c; Zinatloo-Ajabshir et al., 2017), typically the photocatalytic process (Mahdiani et al., 2018; Salavati-Niasari et al., 2016), produces strong oxidizing radicals under light irradiation and degrade macromolecular organics into small molecules (Zheng et al., 2016).

Graphitic carbon nitride (Wen et al., 2017) as a polymeric two-dimensional layered semiconductor has attracted a great interest since 2009 (Wang et al., 2017). It exhibits high chemical and thermal stability, narrow bandgap (~2.7 eV), and potentially high surface area (after exfoliation), which make it highly attractive in the photocatalytic water splitting (Che et al., 2017; Yan et al., 2009), CO₂ reduction (Shi et al., 2018), N₂ fixation (Ma et al., 2016), and organic contaminant degradation (Dai et al., 2014; Oh et al., 2017). Nevertheless, when used as a single component photocatalyst, the performance of g-C₃N₄ is generally limited by its fast recombination of

* This paper has been recommended for acceptance by Dr. Sarah Harmon.

* Corresponding author.

E-mail addresses: pushengyan@gmail.com, pushengyan13@cdut.cn (S. Pu).

electrons and holes (Zhu et al., 2017). A hybridization of g-C₃N₄ with a second semiconductor, such as TiO₂ (Tong et al., 2015; Wei et al., 2017), Ag₃PO₄ (Wang et al., 2014), CdS (Fan et al., 2016), BiVO₄ (Deng et al., 2018), etc. usually induces a spatial separation of electrons and holes with prolonged lifetimes, thus enhancing the photocatalytic preference.

Molybdenum trioxide (MoO₃), as a visible light responsive semiconductor, has been frequently selected to improve the activity of g-C₃N₄ (Feng et al., 2017; He et al., 2014; Huang et al., 2013; Li et al., 2015; Xie et al., 2018; Zhang et al., 2018a). For instance, a g-C₃N₄ shell was coated on the surface of MoO₃ microparticles to form a conventional Type-II heterojunction (Huang et al., 2013). Under a light irradiation, both semiconductors are excited. The photoelectrons tend to accumulate on the conduction band of MoO₃ (more positive) while the holes prefer to concentrate on the valence band of MoO₃ (more negative), thus lowering the overall redox ability of the hybrid. In contrast, a completely different path, i.e. a Z-Scheme transfer, has been suggested for MoO₃/g-C₃N₄ systems by many other groups (Feng et al., 2017; He et al., 2014; Ma et al., 2017; Patnaik et al., 2018). In that case, the electrons in the conduction band of MoO₃ recombine with the holes in the valence band of g-C₃N₄, and the rest holes and electrons maintain their high redox ability (Zhang et al., 2018a). Although radical scavenge experiments (Feng et al., 2017; Li et al., 2015) and/or ESR spin-trap spectra (Xie et al., 2018; Zhang et al., 2018a) have been adopted to prove the type of charge transfer, a more convincing and comprehensive confirmation of the Z-Scheme transfer and the correlation between charge transfer and radical formation are demanded. Moreover, the role of different radicals in photocatalytic dye degradation still need to be clarify. For instance, ·OH has been regarded as the active radicals in many systems (Liu et al., 2016a; Liu et al., 2016b), including Flg-C₃N₄/α-MoO₃ NNs (Zhang et al., 2018b), yet, negligible activity of ·OH in dye degradation by MoO₃/g-C₃N₄ have also been reported by many other groups based on radical scavenge experiments (Liu et al., 2016; Ma et al., 2017; Patnaik et al., 2018; Xie et al., 2018; Zhang et al., 2018a).

In this study, a series of MoO₃/g-C₃N₄ composites with different Mo loadings are prepared through a mixing - annealing method. The combination of MoO₃ and g-C₃N₄ remarkably enhances the photocatalytic activity in dye degradation, compared to pure g-C₃N₄ and MoO₃ as well as a MoO₃/g-C₃N₄ physical mixture. The charge transfer path is studied by applying various techniques, especially ESR spin-trap spectra and radical scavenge experiments, and the reactivity of ·OH is carefully addressed.

2. Experimental section

2.1. Materials

Urea was purchased from US Promega Corporation. Isopropanol ((CH₃)₂CHOH, ≥ 99.7%), benzoquinone (C₆H₄O₂, AR grade), triethanolamine ((HOCH₂CH₂)₃N, ≥ 99.0%), rhodamine B (C₂₈H₃₁ClN₂O₃, ≥ 95%), methylene blue (C₁₆H₁₈ClN₃S·3H₂O, ≥ 82%), safranine T (C₂₀H₁₉ClN₄, ≥ 80%), and methyl blue (C₃₇H₂₇N₃Na₂O₉S₃), molybdenum (VI) oxide (MoO₃, AR grade), sodium sulfate anhydrous (Na₂SO₄, AR grade), and Nafion (AR grade) were purchased from Sigma-Aldrich Chemical Co (USA). Deionized (DI) water and ethanol were purchased from Sigma-Aldrich (molecular biology reagent). All reagents were used without further purification.

2.2. Preparation of MoO₃/g-C₃N₄ composites

g-C₃N₄ (CN) was synthesized according to a previously reported

method (Li et al., 2018). Typically, 10 g of urea was placed into a 20 mL alumina crucible with a cover, and then it was heated up to 550 °C in a muffle furnace at a ramp of 15 °C min⁻¹, and then kept at this temperature for 4 h. After cooling to room temperature, the obtained yellow g-C₃N₄ was collected and ground for further use.

The MoO₃/g-C₃N₄ composites were prepared by mixing MoO₃/g-C₃N₄ followed by a calcination process (Xie et al., 2018). 4 mg to 17.3 mg of MoO₃ and 98 mg g-C₃N₄, with a target MoO₃ loading from 3.9 wt% to 15 wt%, were dispersed into 40 mL of ethanol, then the mixture was sonicated for 1 h and dried at 65 °C under a stirring. The obtained MoO₃/g-C₃N₄ powder was then placed into an alumina crucible with a cover and calcined at 300 °C in air for 4 h in a muffle furnace. The samples were named xMo-CN (x = 3.9, 7.5, or 15) for short. A MoO₃-g-C₃N₄ physical mixture with a MoO₃ loading of 7.5 wt% was prepared by grinding the powders for 5 min.

2.3. Characterization

X-ray diffraction (XRD) was performed with a PANalytical X'pert MPD Pro at 45 kV and 30 mA, using Cu K α radiation at a scanning rate of 3° min⁻¹ in the 2θ range from 5° to 60°. The morphology of the prepared sample was obtained by scanning electron microscope (SEM) with an FEL XL-30FEG (acceleration voltage at 10 kV). Fourier-transform infrared spectroscopy (FTIR) spectra were measured by Nicolet IS50 FTIR Spectrometer in the wavenumber range from 4000 to 500 cm⁻¹. X-ray photoelectron spectroscopy (XPS) was performed on a PHI Quantera XPS with Mg K α radiation as the excitation source. The UV-vis diffuse reflectance spectroscopy (UV-vis DRS) was recorded on a Hitachi UV-vis Spectrophotometer U-2001 using BaSO₄ as the reference. ESR was measured by EMX-8 spectrometer (Bruker BioSpin Corp., Karlsruhe, Germany) with 5,5-dimethyl-1-pyrroline-N-oxide (DMPO) as the spin-trapping agent. Typically, 100 mM of DMPO was added to a methanol (·O₂) or aqueous (·OH) dispersion of sample (1 mg mL⁻¹), and the ESR signals were collected in-situ during the light irradiation.

2.4. Photoelectrochemical measurements

Electrochemical measurement was performed in a three-electrode system with a platinum (Pt) wire as the counter electrode, a Ag/AgCl electrode as the reference electrode, and with an aqueous Na₂SO₄ (0.5 M) as the electrolyte. The working electrode was fabricated through an ink coating process. 10 mg of catalyst was dispersed into 1 mL of ethanol and 20 μL of Nafion. Then the mixture was sonicated for 1 h and magnetically stirred overnight to get a homogeneous ink. Then, 50 μL of the ink was coated onto a 1.0 cm × 1.5 cm fluorine-doped tin oxide (FTO) plate and dried in a muffle furnace at 120 °C for 1 h. A 500 W Xenon lamp equipped with a Newport Solar Simulator AM 1.5G filter was used as the solar simulator.

2.5. Photocatalytic experiment

The photocatalytic RhB degradation was tested under a solar simulator with a power density of 100 mW cm⁻². 25 mg of catalyst was dispersed into 50 mL of RhB solution (10 mg L⁻¹) by sonication, then it was stirred in dark for 30 min to achieve an adsorption-desorption equilibrium. During the test, 2 mL of the suspension was collected at certain time intervals and analyzed with an UV-vis spectrometer (UV-2450, Shimadzu) after removing the solid catalyst by centrifuge. The concentration of RhB was evaluated based on the absorption band peak at around 554 nm. The methylene blue (MB), safranine T (ST), and methyl blue (Mb) degradation were tested with the same procedures except using

solution of 10 mg L^{-1} and checking the absorption band maximum at 665 nm , 530 nm and 660 nm , respectively.

3. Results and discussion

XRD results are shown in Fig. 1a. The as-prepared CN exhibits two broad peaks at 2θ of 12.7° and 27.4° , which ascribe to the in-plane structural packing motifs (indexed as (100)) and the interlayer stacking of conjugated aromatic systems (indexed as (002)) (Masih et al., 2017), respectively. The broad peaks suggest a poor crystallinity and/or a limited thickness of the sample. By adding the commercial MoO_3 , several sharp peaks at 12.9° , 23.4° , 25.7° , 27.3° , 33.8° and 39.1° appear, indicating an orthorhombic structure (JCPDF 35–0609) (Feng et al., 2017) and a bulk feature of the MoO_3 particles. The intensity of the MoO_3 patterns is enhanced gradually with an increase of the MoO_3 content from 3.9 wt% to 15 wt%; meanwhile, the CN patterns are basically maintained.

Fig. 1b shows the FTIR spectra of CN and xMo-CN. All the samples exhibit a broad shoulder at $3300\text{--}3000 \text{ cm}^{-1}$, which is from the stretching modes of C-OH and/or N-H (Wang et al., 2013). Characteristic peaks of g-C₃N₄ are present in the range of $1750\text{--}800 \text{ cm}^{-1}$: the strong peaks at $1750\text{--}1000 \text{ cm}^{-1}$ are ascribed to the emblematic aromatic stretching vibrations of C-N and the typical C=N heterocycles while the peak at 810 cm^{-1} is assigned to the triazine units (Xie et al., 2018). No additional peaks related to MoO_3 (i.e. the stretching mode of O=Mo, O-Mo₂ and O-Mo₃) (Xie et al., 2018) can be detected with a MoO_3 loading up to 15 wt%. Noteworthy, the characteristic peaks of g-C₃N₄ do not show any significant change, indicating a limited effect of the MoO_3 micro particles on the molecular structure of g-C₃N₄.

According to the SEM results, the pristine CN exhibits a porous

and lamellar structure (Fig. S1), which is basically maintained after the introduction of MoO_3 (Fig. 1c). Micro-sized MoO_3 particles ($1\text{--}10 \mu\text{m}$) can be observed in the 7.5Mo-CN composite with their surface decorated with fluffy g-C₃N₄ nanosheets (Fig. 1c). However, a significant portion of the nanosheets shows no contact with MoO_3 due to the large particle size, small surface area, and limited content of MoO_3 . HRTEM has also been tested (Fig. 1d). The nanocrystals with lattice spacing of 0.351 nm and 0.196 nm match, respectively, to the (040) and (061) of MoO_3 (He et al., 2014; Huang et al., 2013), while the g-C₃N₄ around them exhibits no lattice fringes. The crystallinity of these two materials are in a good agreement with the XRD results.

BET analysis shows that the addition of MoO_3 microparticles leads to a significant decrease of the specific surface area from $138.59 \text{ m}^2 \text{ g}^{-1}$ (CN) to $63.27 \text{ m}^2 \text{ g}^{-1}$ (7.5 Mo-CN). It is probably caused by the big MoO_3 microparticles or by the calcination process.

The surface chemical composition and chemical states are analyzed by XPS. As shown in Fig. 2a, two carbon species are present in both CN and 7.5Mo-CN. The main peak at $288.2\text{--}288.4 \text{ eV}$ is from the N-C=N carbon (Xu et al., 2013) while the small one at 284.8 eV is from the C-C/C=C species (Gao et al., 2017). In terms of N, the three peaks at 398.7 eV , 400.2 eV and 401.3 eV correspond to C-N=C, N-(C)₃, and N-H species (Gao et al., 2017), respectively (Fig. 2b). An evident decrease of the N-H and C-N=C species, related to N-(C)₃, indicates a removal of edge N atoms after the Mo loading (Huang et al., 2015). Such structural defects have been reported to trap photoelectrons (Zhang et al., 2018a; Zhu et al., 2018). The commercial MoO_3 is also analyzed and it displays two doublets at the binding energies of $236.6/233.4 \text{ eV}$ and $235.1/232.0 \text{ eV}$, respectively. The main doublet at $236.6/233.4 \text{ eV}$ correspond to Mo^{6+} (~95%), while the latter is ascribed to Mo^{5+} species (He et al., 2014). After the combination with CN, only one doublet exists at

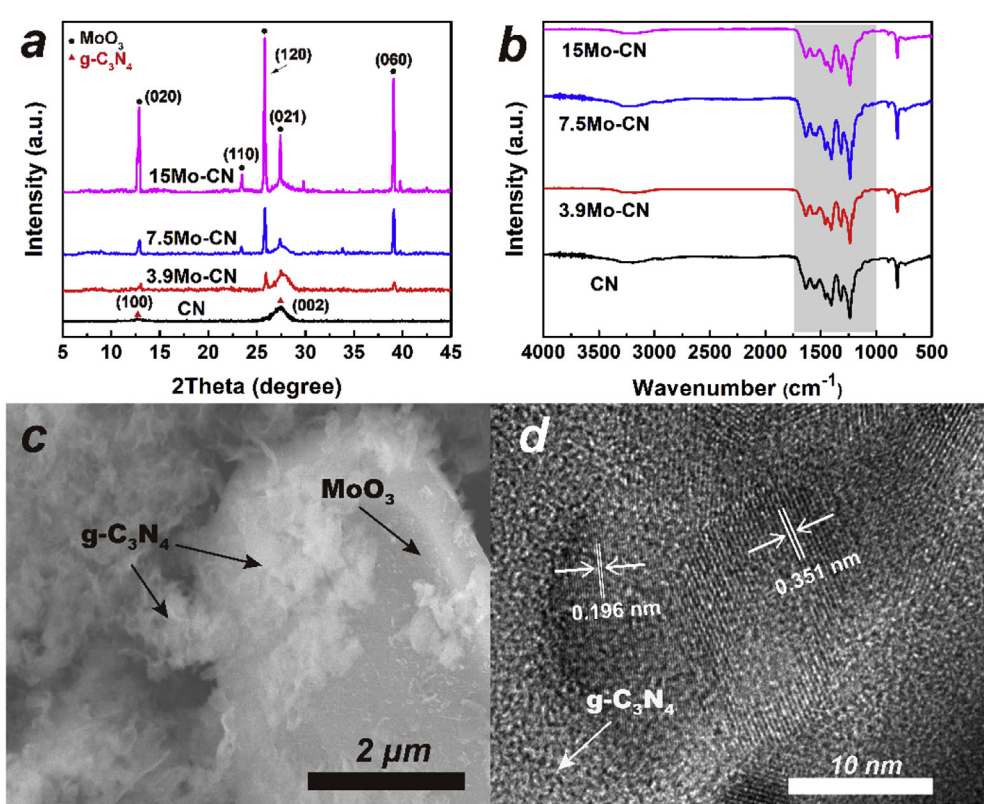


Fig. 1. (a) XRD patterns and (b) FTIR spectrums of CN and xMo-CN composites; SEM image of (c) 7.5Mo-CN and TEM image (d) 7.5Mo-CN.

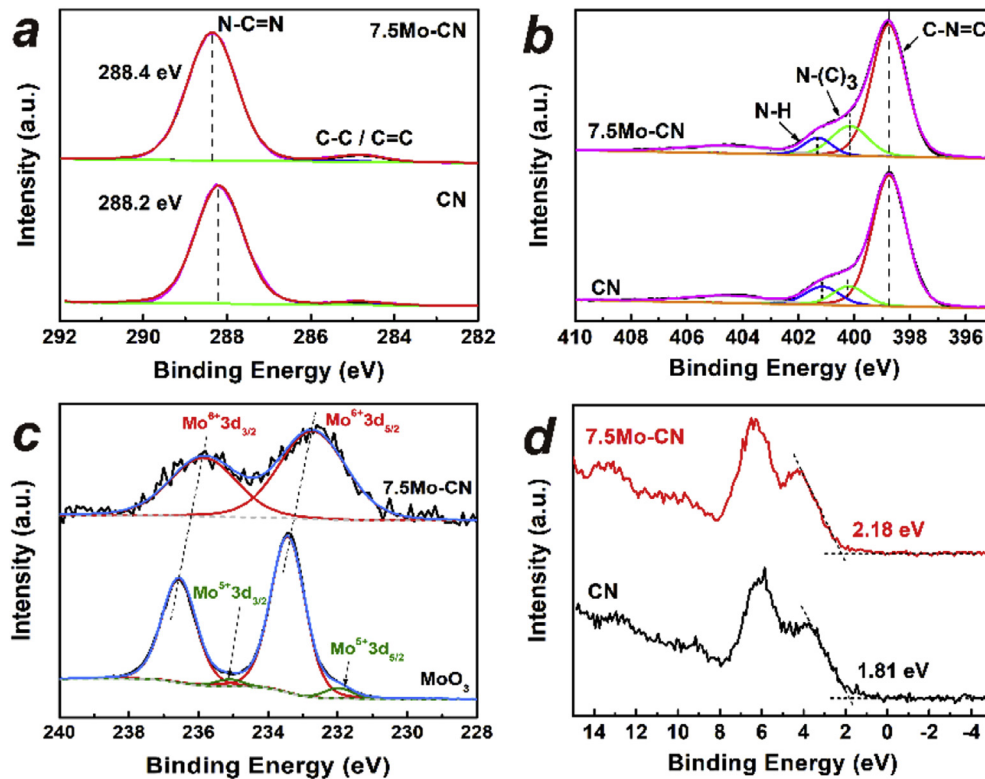


Fig. 2. XPS spectra of CN and 7.5Mo-CN: (a) C1s; (b) N1s; (c) Mo3d. (d) The XPS valence bands of CN and 7.5Mo-CN.

235.9/232.7 eV. Regarding the calcination treatment in air, the Mo in 7.5Mo-CN is proposed to be oxidized to Mo^{6+} . The big shift of binding energy to lower values indicates that the MoO_3 microparticles are chemically bound with the g- C_3N_4 , thanks to their intimate contact (Xie et al., 2018). As expected, the bonding energy of C in g- C_3N_4 slightly shifts to the opposite side (i.e. to higher binding energies) after the loading of MoO_3 . The less shift of C (and N) compared with Mo is probably due to the prevalence of bare g- C_3N_4 without in contact with the MoO_3 microparticles (as confirmed by SEM in Fig. 1c). The XPS-valence bands of CN and MoO_3 are evaluated and it turns out a position of 1.83 eV and 3.67 eV, for CN and MoO_3 , respectively (Fig. 2d).

The optical absorbance properties of CN, MoO_3 and 7.5Mo-CN are measured by UV-vis DRS (Fig. 3a). All the three samples show absorption edges at around 450 nm. The bandgaps of CN, 7.5Mo-CN and

MoO_3 , obtained from the Kubelka-Munk plots (Otsuka, 2004), are 2.84, 2.81, and 2.74 eV, respectively (Fig. 3b). Basically, the addition of MoO_3 has a very limited impact on the light absorption.

The photocatalytic activities of all the samples in RhB degradation are shown in Fig. 4a. In the absence of a photocatalyst, no degradation of RhB is observed under the light irradiation, thus ruling out the self-degradation of RhB. The MoO_3 alone shows no activity, while the pure CN degrades more than 60% of the RhB within 25 min. The incorporation of the inactive MoO_3 significantly enhances the overall activity, and the RhB can be completely degraded within 10–15 min based on the UV-vis spectra (Fig. S2). A blue shift of absorption peak of RhB solution from 554 nm to 495 nm indicates a N-demethylation process during the degradation of RhB (Liu et al., 2017b). By increasing the content of MoO_3 from 0 to 15 wt%, the activity shows a volcano-shaped trend and

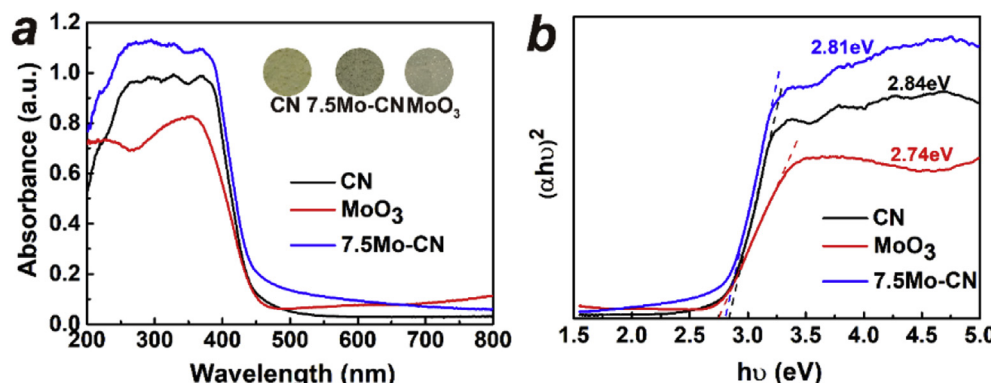


Fig. 3. (a) UV-Vis DRS and (b) the related bandgaps of CN, 7.5Mo-CN and MoO_3 . Inset are the colors of the three samples. (For interpretation of the references to color in this figure legend, the reader is referred to the Web version of this article.)

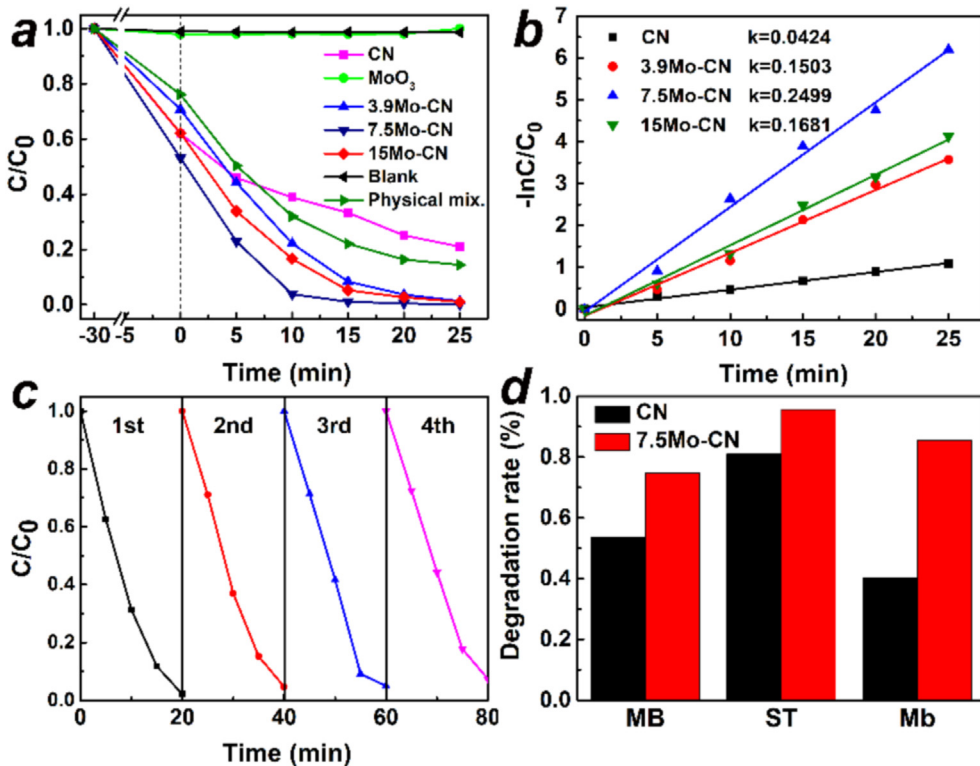


Fig. 4. (a) Photocatalytic activities of different samples in RhB degradation and (b) the related kinetic comparison; (c) the recyclability test of 7.5Mo-CN for the degradation of RhB. Conditions: content of photocatalyst: 0.5 g L⁻¹; temperature: 298 ± 0.5 K; stirring rate: 180 rpm; initial concentration of RhB: 10 mg L⁻¹. (d) Photocatalytic activities of 7.5Mo-CN for MB, ST and Mb degradation. Conditions: content of photocatalyst: 0.5 g L⁻¹; temperature: 298 ± 0.5 K; stirring rate: 180 rpm; initial concentration of MB, ST and Mb: 10 mg L⁻¹.

7.5Mo-CN performs the best. No evident decay of the RhB degradation rate can be observed during the four-cycle tests (Fig. 4c). The sample before and after test are compared in Fig. S3. Although the g-C₃N₄ nanosheets curl during the test, their contact with MoO₃ particles are well maintained according to SEM (Fig. S3 f). The XRD, FTIR and XPS results do not show any big change, confirming the good stability of 7.5Mo-CN. The reaction kinetics of photocatalytic activity are further calculated for a quantitative comparison. All the results are fitted by first-order model as given by the following equation (Liu et al., 2016).

$$-\ln\left(\frac{C_0}{C}\right) = kt \quad (1)$$

where C_0 is the initial concentration of dye, k is the apparent reaction first-order rate constant, C is the concentration of the dye after exposure time of t (Ma et al., 2017). The photocatalytic reaction rate of the samples can be easily compared by the k values. As shown in Fig. 4b, the reaction rate increases from 0.0424 to 0.1503 and 0.2499 min⁻¹ with the addition of MoO₃ from 0% to 3.9 wt% and 7.5 wt%, respectively. A further addition of MoO₃ to 15 wt% causes a decrease of the reaction rate to 0.1681 min⁻¹, which is probably due to the shielding of g-C₃N₄ by MoO₃ (Feng et al., 2017). As a control experiment, a mixture consisting of 7.5 wt% of MoO₃ and 92.5 wt% of CN is prepared by physical grinding. The mixture shows small improvement compared with CN, yet its activity is not comparable with 7.5Mo-CN, despite the same composition (Fig. 4a). The results highlight the role of the strong interaction between the two components in building up a synergy. Moreover, despite the negative impact of MoO₃ addition in lowering the specific surface area, 7.5Mo-CN still outperforms the original CN. The catalysts have been further applied to other dyes, such as methylene blue (MB),

safranine T (ST) and methyl blue (Mb), and in all cases the 7.5Mo-CN performs better (Figs. 4d and S4). Compared with other catalysts, the catalytic activity of the 7.5Mo-CN is better than most of them (Table S1).

3.1. Reaction mechanism

Radical scavenging experiments are firstly carried out to understand the active species. Isopropanol (IPA, 75 mM), triethanolamine (TEOA, 10 mM) and p-benzoquinone (p-BQ, 1 mM) are used as the scavengers for ·OH, hole and ·O₂⁻, respectively (Liu et al., 2017a; Lu et al., 2017). As shown in Fig. 5a, the addition of IPA has a limited impact on the RhB degradation, while the addition of either TEOA or p-BQ largely suppresses the reaction. It indicates a vital role of hole and ·O₂⁻ in catalyzing the degradation of RhB. To further confirm the existence of ·OH and ·O₂⁻ in the system, ESR spin-trap experiment is performed with DMPO as the spin-trapping agent (Liu et al., 2016). The detection of ·O₂⁻ is performed in DI water while the detection of ·OH is performed in methanol. The related products (e.g. DMPO-·O₂⁻ or DMPO-·OH) are characterized by ESR (Ye et al., 2016). As shown in Fig. 5c-d (Ye et al., 2016), neither ·OH nor ·O₂⁻ is produced in dark, while the light irradiation induces a gradual increase of both radicals in both the CN and 7.5Mo-CN systems (Fig. S5). Regarding the negligible impact of IPA (as a ·OH scavenger, shown in Fig. 5a), the existence of ·OH in the system based on ESR proves a low activity of ·OH in RhB degradation. As a proof of concept, the pH value is adjusted to alter the concentration of ·OH in the solution. Generally, pH value affects the photocatalytic reaction by changing the surface charge and the adsorption behavior or by changing the generation of radicals (Rosli et al., 2018; Tao et al., 2015). With a decrease of pH value from 11 to 3, the adsorption capacity of 7.5Mo-CN remains constant, ruling out the

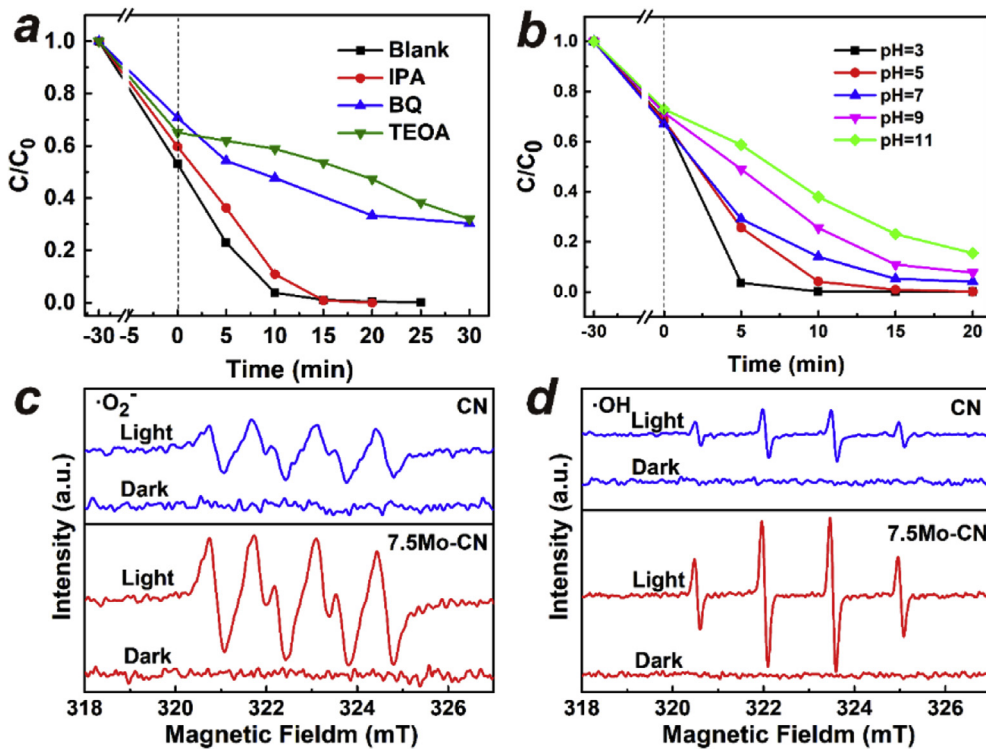


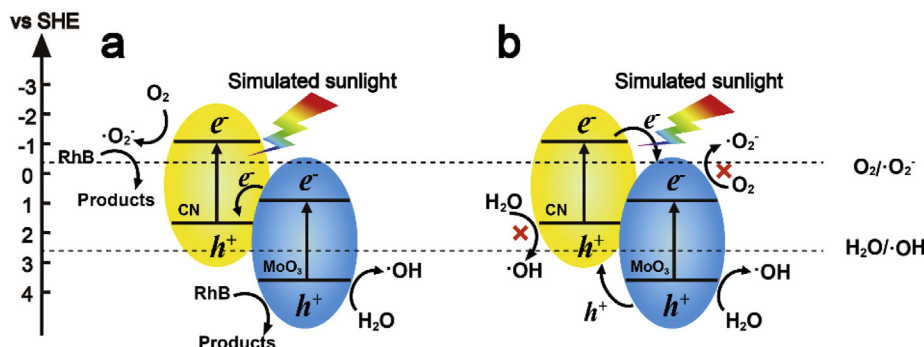
Fig. 5. (a) Photocatalytic activity of 7.5Mo-CN for the degradation of RhB with different scavengers. Conditions: content of photocatalyst: 0.5 g L^{-1} ; IPA: 75 mM ; TEOA: 10 mM ; p-BQ: 1 mM ; temperature: $298 \pm 0.5 \text{ K}$; stirring rate: 180 rpm ; initial concentration of RhB: 10 mg L^{-1} . (b) The effect of pH value in RhB degradation. Conditions: content of photocatalyst: 0.5 g L^{-1} ; temperature: $298 \pm 0.5 \text{ K}$; stirring rate: 180 rpm ; initial concentration of RhB: 10 mg L^{-1} . ESR detections of (c) $\cdot\text{O}_2^-$ and (d) $\cdot\text{OH}$ either in dark or after a light irradiation for 15 min. Conditions: content of photocatalyst: 1 mg mL^{-1} ; DMPO: 100 mM .

former effect, while the photocatalytic activity improves continuously (Fig. 5b). Based on the formation paths of $\cdot\text{OH}$ (i.e. $\text{h}^+ + \text{H}_2\text{O} \rightarrow \cdot\text{OH} + \text{H}^+$ or $\text{h}^+ + \text{OH}^- \rightarrow \cdot\text{OH}$) (Michael R. Hoffmann, 1995; Wen et al., 2017), a higher pH value favors the conversion of holes to $\cdot\text{OH}$. To further confirm the effect of pH value on the conversion of holes, quencher experiments with TEOA (hole scavenger) at pH of 3 and 11 are performed (Fig. S6). In the absence of TEOA, the sample at pH of 3 shows much higher activity than at pH of 11. However, by trapping all the holes with TEOA, the activity at pH of 3 and 11 become similar. Since the activity of hydroxyl radicals is negligible and the degradation of RhB is mainly contributed by holes and superoxide radicals. It is evident that the hole concentration is much higher at pH of 3 than at pH of 11, while the concentration of superoxide radicals does not depend on the pH value. Therefore, the declined activity in basic solutions strongly support our expectation that the produced $\cdot\text{OH}$ are not active for the RhB degradation reaction.

As shown in Fig. 5c–d, 7.5Mo-CN has a higher production efficiency of both radicals compared with CN, in line with its higher photocatalytic activity. To understand this phenomenon, the energy diagram of this heterojunction is prepared. According to bandgaps and the valence band positions, obtained from UV-vis DRS and XPS-VB, respectively, CN has a conduction band of -1.01 eV and a valence band of 1.83 eV , while MoO₃ has a conduction band of 0.93 eV and a valence band of 3.67 eV (shown in Scheme 1). Generally, $\cdot\text{O}_2^-$ is produced via a reduction of O₂ with the photogenerated electrons ($e^- + \text{O}_2 \rightarrow \cdot\text{O}_2^-$, $\text{O}_2/\cdot\text{O}_2^- = -0.33 \text{ V}$ vs. NHE) (Michael R. Hoffmann, 1995; Wen et al., 2017). The conduction band electrons in MoO₃ are thermodynamically not active to produce $\cdot\text{O}_2^-$. Thus, the higher concentration of $\cdot\text{O}_2^-$ in the 7.5Mo-CN system indicates a better accumulation of electrons in the conduction band of CN, rather than MoO₃. In terms of $\cdot\text{OH}^-$, it can

be either directly produced by an oxidation of H₂O with holes ($\text{h}^+ + \text{H}_2\text{O} \rightarrow \cdot\text{OH} + \text{H}^+$, $\cdot\text{OH}/\text{OH}^- = 2.40 \text{ V}$ vs. NHE) (Michael R. Hoffmann, 1995; Wen et al., 2017) or come indirectly from $\cdot\text{O}_2^-$ through a series of reactions ($\cdot\text{O}_2^- + \text{H}_2\text{O} \rightarrow \text{H}_2\text{O}_2 \rightarrow \cdot\text{OH}$) (Michael R. Hoffmann, 1995; Wen et al., 2017). Since the valence band of g-C₃N₄ (i.e. 1.83 eV) is not positive enough to produce $\cdot\text{OH}^-$ directly, the $\cdot\text{OH}^-$ observed in the pure CN system (Fig. 5d) should be produced through the indirect path. The significantly higher concentration of $\cdot\text{OH}$ in the presence of MoO₃ (i.e. for the 7.5Mo-CN system) is due to a change of the reaction path, i.e. to a direct oxidation of H₂O by the highly oxidative holes in the valence band of MoO₃ ($\text{h}^+ + \text{H}_2\text{O} \rightarrow \cdot\text{OH} + \text{H}^+$). To summarize, the accumulation of electrons in the conduction band of CN while holes in the valence band of MoO₃ highly suggests a Z-Scheme type charge transfer (Zhang et al., 2018a) (Scheme 1a). Under the light irradiation, both MoO₃ and g-C₃N₄ are excited. The photoelectrons in the conduction band of MoO₃ tend to recombine with the holes in the valence band of g-C₃N₄, thanks to the small gap (i.e. 0.90 eV). The left electrons in the conduction band of g-C₃N₄ are relatively stable thus continuously reduce O₂ to $\cdot\text{O}_2^-$. The holes in the valence band of MoO₃ partially contribute to the oxidation of dyes, while the rest holes are converted to $\cdot\text{OH}$, which however is not reactive for RhB. In term of a conventional Type-II heterojunctions, the charge transfer from the high energy conduction band and valence band to the lower energy ones will lead to a decline of both $\cdot\text{O}_2^-$ and $\cdot\text{OH}$ concentrations (Scheme 1b), which however is not the case of our system.

Photoelectrochemical experiments are conducted to investigate the formation, separation and transfer of the photocarriers (Guo et al., 2018). As shown in Fig. 6a, the two samples show stable photocurrent under light illumination, and the photocurrent intensity of 7.5Mo-CN is ~ 1.8 times higher than CN, indicating a boost of photocarriers with the addition of MoO₃. The electrochemical



Scheme 1. (a) Z-Scheme charge transfer; (b) conventional charge transfer.

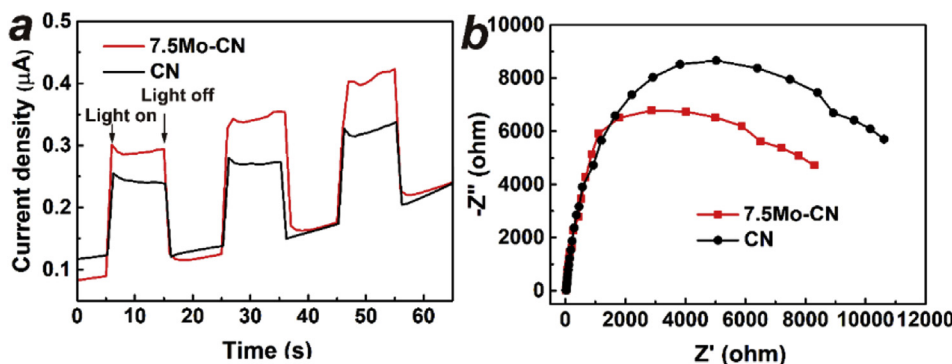


Fig. 6. (a) Photocurrent responses and (b) EIS spectra of CN and 7.5Mo-CN. Electrode preparation: 10 mg catalyst; 1 mL of ethanol, and 20 μL of Nafion.

impedance spectroscopy (EIS) measurements (Fig. 6b) give a smaller diameter of the semicircular Nyquist plot for 7.5Mo-CN, suggesting a lower charge transfer resistance. Despite the imperfection of the selected commercial MoO₃ microparticles in terms of their large sizes and limited interface with the g-C₃N₄ nanosheets, the partially formed heterostructure still effectively separate the photoexcited electron-hole pairs and enhance the photocatalytic activity.

4. Conclusions

In summary, a series of MoO₃/g-C₃N₄ hetero-structured photocatalysts have been prepared by a mixing - annealing method, which results in a strong interaction between the two components as well as a synergistic effect in the photocatalytic dye degradations. The photocatalytic enhancement is caused by a direct Z-scheme interparticle charge transfer, which not only facilitates the separation of electron-hole pairs but also thermodynamically favors the formation of active ·O₂⁻ radicals and holes. This research provides a more convincing and comprehensive certificate of the charge transfer path in the MoO₃/g-C₃N₄ system by applying the ESR spin-trap spectra, radical scavenge experiments, photoelectrochemical analysis and so on. It builds up a correlation between the charge transfer paths and the radical formations and proves the poor reactivity of ·OH in RhB degradations. In addition, the work provides a concept to control the formation of active radicals by properly designing the heterostructures and by changing the reaction conditions, such as pH value.

Notes

The authors declare that there is no conflict of interests

regarding the publication of this paper.

Acknowledgements

This work was supported by the National Natural Science Foundation of China (No. 41772264), the Applied Basic Research Programs of Science and Technology Foundation of Sichuan Province (18YYJC1745) and the Research Fund of State Key Laboratory of Geohazard Prevention and Geoenvironment Protection (SKLGP2018Z001).

Appendix A. Supplementary data

Supplementary data to this article can be found online at <https://doi.org/10.1016/j.envpol.2019.04.010>.

References

- Aljuboori, A.H., Idris, A., Al-joubory, H.H., Uemura, Y., Ibn Abubakar, B.S., 2015. Flocculation behavior and mechanism of bioflocculant produced by *Aspergillus flavus*. *J. Environ. Manag.* 150, 466–471.
- Che, W., Cheng, W.R., Yao, T., Tang, F.M., Liu, W., Su, H., Huang, Y.Y., Liu, Q.H., Liu, J.K., Hu, F.C., Pan, Z.Y., Sun, Z.H., Wei, S.Q., 2017. Fast photoelectron transfer in (C-ring)-C₃N₄ plane heterostructural nanosheets for overall water splitting. *J. Am. Chem. Soc.* 139, 3021–3026.
- Dai, K., Lu, L., Liang, C., Liu, Q., Zhu, G., 2014. Heterojunction of facet coupled g-C₃N₄/surface-fluorinated TiO₂ nanosheets for organic pollutants degradation under visible LED light irradiation. *Appl. Catal. B Environ.* 156–157, 331–340.
- de Araujo, D.M., Saez, C., Martinez-Huitle, C.A., Canizares, P., Rodrigo, M.A., 2015. Influence of mediated processes on the removal of Rhodamine with conductive-diamond electrochemical oxidation. *Appl. Catal. B Environ.* 166, 454–459.
- Deng, Y., Tang, L., Feng, C., Zeng, G., Wang, J., Zhou, Y., Liu, Y., Peng, B., Feng, H., 2018. Construction of plasmonic Ag modified phosphorous-doped ultrathin g-C₃N₄ nanosheets/BiVO₄ photocatalyst with enhanced visible-near-infrared response ability for ciprofloxacin degradation. *J. Hazard Mater.* 344, 758–769.
- Fan, Q.J., Huang, Y.N., Zhang, C., Liu, J.J., Piao, L.Y., Yu, Y.C., Zuo, S.L., Li, B.S., 2016.

- Superior nanoporous graphitic carbon nitride photocatalyst coupled with CdS quantum dots for photodegradation of RhB. *Catal. Today* 264, 250–256.
- Feng, Z., Zeng, L., Chen, Y.J., Ma, Y.Y., Zhao, C.R., Jin, R.S., Lu, Y., Wu, Y., He, Y.M., 2017. In situ preparation of Z-scheme MoO₃/g-C₃N₄ composite with high performance in photocatalytic CO₂ reduction and RhB degradation. *J. Mater. Res.* 32, 3660–3668.
- Gao, J.T., Wang, Y., Zhou, S.J., Lin, W., Kong, Y., 2017. A facile one-step synthesis of Fe-doped g-C₃N₄ nanosheets and their improved visible-light photocatalytic performance. *ChemCatChem* 9, 1708–1715.
- Grandclément, C., Seyssieq, I., Piram, A., Wong-Wah-Chung, P., Vanot, G., Tiliacos, N., Roche, N., Doumenq, P., 2017. From the conventional biological wastewater treatment to hybrid processes, the evaluation of organic micropollutant removal: a review. *Water Res.* 111, 297–317.
- Guo, F., Shi, W.L., Zhu, C., Li, H., Kang, Z.H., 2018. CoO and g-C₃N₄ complement each other for highly efficient overall water splitting under visible light. *Appl. Catal. B Environ.* 226, 412–420.
- He, Y.M., Zhang, L.H., Wang, X.X., Wu, Y., Lin, H.J., Zhao, L.H., Weng, W.Z., Wan, H.L., Fan, M.H., 2014. Enhanced photodegradation activity of methyl orange over Z-scheme type MoO₃-g-C₃N₄ composite under visible light irradiation. *RSC Adv.* 4, 13610–13619.
- Huang, L.Y., Xu, H., Zhang, R.X., Cheng, X.N., Xia, J.X., Xu, Y.G., Li, H.M., 2013. Synthesis and characterization of g-C₃N₄/MoO₃ photocatalyst with improved visible-light photoactivity. *Appl. Surf. Sci.* 283, 25–32.
- Huang, Z.a., Sun, Q., Lv, K., Zhang, Z., Li, M., Li, B., 2015. Effect of contact interface between TiO₂ and g-C₃N₄ on the photoreactivity of g-C₃N₄/TiO₂ photocatalyst: (001) vs (101) facets of TiO₂. *Appl. Catal. B Environ.* 164, 420–427.
- Li, X., Sun, X., Zhang, L., Sun, S., Wang, W., 2018. Efficient photocatalytic fixation of N₂ by KOH-treated g-C₃N₄. *J. Mater. Chem. B*, 6, 3005–3011.
- Li, Y.P., Huang, L.Y., Xu, J.B., Xu, H., Xu, Y.G., Xia, J.X., Li, H.M., 2015. Visible-light-induced blue MoO₃-C₃N₄ composite with enhanced photocatalytic activity. *Mater. Res. Bull.* 70, 500–505.
- Liao, Y., Loh, C.-H., Tian, M., Wang, R., Fane, A.G., 2018. Progress in electrospun polymeric nanofibrous membranes for water treatment: fabrication, modification and applications. *Prog. Polym. Sci.* 77, 69–94.
- Liu, Q., Chen, T., Guo, Y., Zhang, Z., Fang, X., 2017a. Grafting Fe(III) species on carbon nanodots/Fe-doped g-C₃N₄ via interfacial charge transfer effect for highly improved photocatalytic performance. *Appl. Catal. B Environ.* 205, 173–181.
- Liu, Q., Guo, Y.R., Chen, Z.H., Zhang, Z.G., Fang, X.M., 2016. Constructing a novel ternary Fe(III)/graphene/g-C₃N₄ composite photocatalyst with enhanced visible-light driven photocatalytic activity via interfacial charge transfer effect. *Appl. Catal. B Environ.* 183, 231–241.
- Liu, T., Wang, L., Lu, X., Fan, J., Cai, X., Gao, B., Miao, R., Wang, J., Lv, Y., 2017b. Comparative study of the photocatalytic performance for the degradation of different dyes by ZnIn₂S₄: adsorption, active species, and pathways. *RSC Adv.* 7, 12292–12300.
- Lu, N., Wang, C.Y., Sun, B., Gao, Z.M., Su, Y., 2017. Fabrication of TiO₂-doped single layer graphitic-C₃N₄ and its visible-light photocatalytic activity. *Separ. Purif. Technol.* 186, 226–232.
- Ma, H.Q., Shi, Z.Y., Li, S., Liu, N., 2016. Large-scale production of graphitic carbon nitride with outstanding nitrogen photofixation ability via a convenient microwave treatment. *Appl. Surf. Sci.* 379, 309–315.
- Ma, L.N., Dong, X.F., Chen, M.L., Zhu, L., Wang, C.X., Yang, F.L., Dong, Y.C., 2017. Fabrication and water treatment application of carbon nanotubes (CNTs)-Based composite membranes: a review. *Membranes* 7, 21.
- Mahdiani, M., Soofivand, F., Ansari, F., Salavati-Niasari, M., 2018. Grafting of CuFe₁₂O₁₉ nanoparticles on CNT and graphene: eco-friendly synthesis, characterization and photocatalytic activity. *J. Clean. Prod.* 176, 1185–1197.
- Masih, D., Ma, Y., Rohani, S., 2017. Graphitic C₃N₄ based noble-metal-free photocatalyst systems: a review. *Appl. Catal. B Environ.* 206, 556–588.
- Merkulov, D.V.S., Despotovic, V.N., Banic, N.D., Armakovic, S.J., Fincur, N.L., Lazarevic, M.J., Cetovic-Simin, D.D., Orcic, D.Z., Radoicic, M.B., Saponjic, Z.V., Comor, M.I., Abramovic, B.F., 2018. Photocatalytic decomposition of selected biologically active compounds in environmental waters using TiO₂/polyaniline nanocomposites: kinetics, toxicity and intermediates assessment. *Environ. Pollut.* 239, 457–465.
- Hoffmann, Michael R., M. S.T., Choi, Wonyong, Bahnenmann, Detlef W., 1995. Environmental applications of semiconductor photocatalysis. *Chem. Rev.* 95, 69–96.
- Oh, W.D., Chang, V.W.C., Hu, Z.T., Goei, R., Lim, T.T., 2017. Enhancing the catalytic activity of g-C₃N₄ through Me doping (Me = Cu, Co and Fe) for selective sulfathiazole degradation via redox-based advanced oxidation process. *Chem. Eng. J.* 323, 260–269.
- Otsuka, M., 2004. Comparative particle size determination of phenacetin bulk powder by using Kubelka–Munk theory and principal component regression analysis based on near-infrared spectroscopy. *Powder Technol.* 141, 244–250.
- Patnaik, S., Swain, G., Parida, K.M., 2018. Highly efficient charge transfer through a double Z-scheme mechanism by a Cu-promoted MoO₃/g-C₃N₄ hybrid nanocomposite with superior electrochemical and photocatalytic performance. *Nanoscale* 10, 5950–5964.
- Pu, S., Wang, M., Wang, K., Hou, Y., Yu, J., Shi, Q., Pei, X., Chu, W., 2017a. Preparation of CS-Fe@Fe₃O₄ nanocomposite as an efficient and recyclable adsorbent for azo dyes removal. *Desalination Water Treat.* 95, 319–332.
- Pu, S., Xiang, C., Zhu, R., Ma, H., Zinchenko, A., Chu, W., 2017b. An efficient heterogeneous Fenton catalyst based on modified diatomite for degradation of cationic dye simulated wastewater. *Desalination Water Treat.* 79, 378–385.
- Pu, S., Xue, S., Yang, Z., Hou, Y., Zhu, R., Chu, W., 2018. In situ co-precipitation preparation of a superparamagnetic graphene oxide/Fe₃O₄ nanocomposite as an adsorbent for wastewater purification: synthesis, characterization, kinetics, and isotherm studies. *Environ. Sci. Pollut. Control Ser.* 25, 17310–17320.
- Pu, S., Zhu, R., Ma, H., Deng, D., Pei, X., Qi, F., Chu, W., 2017c. Facile in-situ design strategy to disperse TiO₂ nanoparticles on graphene for the enhanced photocatalytic degradation of rhodamine 6G. *Appl. Catal. B Environ.* 218, 208–219.
- Rosli, N.I.M., Lam, S.M., Sin, J.C., Satoshi, I., Mohamed, A.R., 2018. Photocatalytic performance of ZnO/g-C₃N₄ for removal of phenol under simulated sunlight irradiation. *J. Environ. Eng.* 144.
- Salavati-Niasari, M., Soofivand, F., Sobhani-Nasab, A., Shakouri-Arani, M., Faal, A.Y., Bagheri, S., 2016. Synthesis, characterization, and morphological control of ZnTiO₃ nanoparticles through sol-gel processes and its photocatalyst application. *Adv. Powder Technol.* 27, 2066–2075.
- Shi, G.D., Yang, L., Liu, Z.W., Chen, X., Zhou, J.Q., Yu, Y., 2018. Photocatalytic reduction of CO₂ to CO over copper decorated g-C₃N₄ nanosheets with enhanced yield and selectivity. *Appl. Surf. Sci.* 427, 1165–1173.
- Tao, Y., Ni, Q., Wei, M., Xia, D., Li, X., Xu, A., 2015. Metal-free activation of peroxymonosulfate by g-C₃N₄ under visible light irradiation for the degradation of organic dyes. *RSC Adv.* 5, 44128–44136.
- Tong, Z., Yang, D., Xiao, T., Tian, Y., Jiang, Z., 2015. Biomimetic fabrication of g-C₃N₄/TiO₂ nanosheets with enhanced photocatalytic activity toward organic pollutant degradation. *Chem. Eng. J.* 260, 117–125.
- Wang, W., Fang, J.J., Shao, S.F., Lai, M., Lu, C.H., 2017. Compact and uniform TiO₂@g-C₃N₄ core-shell quantum heterojunction for photocatalytic degradation of tetracycline antibiotics. *Appl. Catal. B Environ.* 217, 57–64.
- Wang, W., Yu, J.C., Xia, D., Wong, P.K., Li, Y., 2013. Graphene and g-C₃N₄ nanosheets cowrapped elemental alpha-sulfur as a novel metal-free heterojunction photocatalyst for bacterial inactivation under visible-light. *Environ. Sci. Technol.* 47, 8724–8732.
- Wang, Y.F., Liu, J.X., Wang, Y.W., Fan, C.M., Ding, G.Y., 2014. Regeneration of novel visible-light-driven Ag/Ag₃PO₄@C₃N₄ hybrid materials and their high photocatalytic stability. *Mater. Sci. Semicond. Process.* 25, 330–336.
- Wei, Z., Liang, F., Liu, Y., Luo, W., Wang, J., Yao, W., Zhu, Y., 2017. Photoelectrocatalytic degradation of phenol-containing wastewater by TiO₂/g-C₃N₄ hybrid heterostructure thin film. *Appl. Catal. B Environ.* 201, 600–606.
- Wen, J.Q., Xie, J., Chen, X.B., Li, X., 2017. A review on g-C₃N₄-based photocatalysts. *Appl. Surf. Sci.* 391, 72–123.
- Xie, Z.J., Feng, Y.P., Wang, F.L., Chen, D.N., Zhang, Q.X., Zeng, Y.Q., Lv, W.Y., Liu, G.G., 2018. Construction of carbon dots modified MoO₃/g-C₃N₄ Z-scheme photocatalyst with enhanced visible-light photocatalytic activity for the degradation of tetracycline. *Appl. Catal. B Environ.* 229, 96–104.
- Xu, J., Zhang, L., Shi, R., Zhu, Y., 2013. Chemical exfoliation of graphitic carbon nitride for efficient heterogeneous photocatalysis. *J. Mater. Chem. I*, 1, 14766.
- Yan, S.C., Li, Z.S., Zou, Z.G., 2009. Photodegradation performance of g-C₃N₄ fabricated by directly heating melamine. *Langmuir* 25, 10397–10401.
- Ye, R., Fang, H., Zheng, Y.Z., Li, N., Wang, Y., Tao, X., 2016. Fabrication of CoTiO₃/g-C₃N₄ hybrid photocatalysts with enhanced H₂ evolution: Z-scheme photocatalytic mechanism insight. *ACS Appl. Mater. Interfaces* 8, 13879–13889.
- Zhang, X., Yi, J., Chen, H., Mao, M., Liu, L., She, X., Ji, H., Wu, X., Yuan, S., Xu, H., Li, H., 2018a. Construction of a few-layer g-C₃N₄/α-MoO₃ nanoneedles all-solid-state Z-scheme photocatalytic system for photocatalytic degradation. *J. Energy Chem.* 29, 65–71.
- Zhang, X., Yi, J., Chen, H., Mao, M., Liu, L., She, X., Ji, H., Wu, X., Yuan, S., Xu, H., Li, H., 2018b. Construction of a few-layer g-C₃N₄/α-MoO₃ nanoneedles all-solid-state Z-scheme photocatalytic system for photocatalytic degradation. *J. Energy Chem.* 29, 65–71.
- Zheng, J.-t., Zhu, C.-s., Jiang, B., 2016. Uses of Activated Carbon Fibers and Advanced Oxidation Technologies in the Remediation of Water. *Carbon*, p. 260.
- Zhu, M.S., Kim, S., Mao, L., Fujitsuka, M., Zhang, J.Y., Wang, X.C., Majima, T., 2017. Metal-Free photocatalyst for H₂ evolution in visible to near-infrared region: black phosphorus/graphitic carbon nitride. *J. Am. Chem. Soc.* 139, 13234–13242.
- Zhu, Z., Pan, H., Murugananthan, M., Gong, J., Zhang, Y., 2018. Visible light-driven photocatalytically active g-C₃N₄ material for enhanced generation of H₂O₂. *Appl. Catal. B Environ.* 232, 19–25.
- Zinatloo-Ajabshir, S., Morassaei, M.S., Salavati-Niasari, M., 2017. Facile fabrication of Dy₂Sn₂O₇-SnO₂ nanocomposites as an effective photocatalyst for degradation and removal of organic contaminants. *J. Colloid Interface Sci.* 497, 298–308.